Brownian motion of droplets induced by thermal noise

Haodong Zhang,[1,2] Fei Wang,[1,2,*] Lorenz Ratke,[3] and Britta Nestler[1,4]

[1]*Institute of Applied Materials-Microstructure Modelling and Simulation, Karlsruhe Institute of Technology (KIT), Strasse am Forum 7, 76131 Karlsruhe, Germany*

[2]*Institute of Nanotechnology, Karlsruhe Institute of Technology (KIT), Hermann-von-Helmholtz-Platz 1, 76344 Eggenstein-Leopoldshafen, Germany*

[3]*Institute of Materials Research, German Aerospace Center, Linder Hoehe, 51147 Cologne, Germany*

[4]*Institute of Digital Materials Science, Karlsruhe University of Applied Sciences, Moltkestrasse 30, 76133 Karlsruhe, Germany*

Brownian motion (BM) is pivotal in natural science for the stochastic motion of microscopic droplets. In this study, we investigate BM driven by thermal composition noise at submicro scales, where intermolecular diffusion and surface tension both are significant. To address BM of microscopic droplets, we develop two stochastic multiphase-field models coupled with the full Navier-Stokes equation, namely, Allen-Cahn-Navier-Stokes and Cahn-Hilliard-Navier-Stokes. Both models are validated against capillary-wave theory; the Einstein's relation for the Brownian coefficient $D^* \sim k_B T/r$ at thermodynamic equilibrium is recovered. Moreover, by adjusting the coaction of the diffusion, Marangoni effect, and viscous friction, two nonequilibrium phenomena are observed. (I) The droplet motion transits from the Brownian to Ballistic with increasing Marangoni effect which is emanated from the energy dissipation mechanism distinct from the conventional fluctuation-dissipation theorem. (II) The deterministic droplet motion is triggered by the noise induced nonuniform velocity field which leads to a novel droplet coalescence mechanism associated with the thermal noise.

I. INTRODUCTION

Brownian motion (BM) owes its original observation and nomenclature to Robert Brown [1]. Within the purview of natural sciences, BM characterizes the persistent stochastic motion of droplets suspended within a fluid medium [2,3]. Given its interdisciplinary significance and broad accessibility, BM has not only elicited considerable scientific interest but also found widespread utility in numerous practical applications [4,5]. A salient feature of the droplet BM is the relationship of the Brownian coefficient $D^* \sim k_B T/(\eta\, r_0)$ with the viscosity η and droplet radius r_0. Resulting from this relationship, the droplet mean squared displacement (MSD) increases linearly with time as

$$\langle \Delta X^2 \rangle \sim 2\, D^* t. \tag{1}$$

It is important to note that this relation is based on certain fundamental assumptions. First, it presupposes a rigid droplet without fluid flow inside the droplet. Second, it does not account for the hydrodynamic effects arising from the surface tension, which are particularly pertinent when changes in droplet curvature due to deformation and coalescence are pronounced. Lastly, the mutual interactions between droplets are neglected and only the viscous friction with the surrounding matrix is considered. However, for lots of materials, including but not limited to polymer solutions, aerogels, and hydrogels [6,7], the droplets do not exhibit rigid, solid-body behavior; instead, they manifest as liquid-state entities, often taking the form of droplets via phase separation or nucleation. These droplets assume a paramount role in shaping the microstructural composition of materials, for which the mass diffusion, surface tension effect [8], and hydrodynamics [9] are pivotal. Furthermore, the dispersed droplets engage in interactions and coagulation with one another, rendering the complex process inherently contextualized within a many-body physical framework, which is beyond the scope of the single droplet BM discussed by Einstein [10].

A well-established model for characterizing BM is the Langevin equation [11]. Within this framework, BM is depicted as the motion of a droplet represented as a mass point, propelled by the stochastic force resulting from collisions between the matrix fluid molecules and the Brownian droplets. Meanwhile, this motion is counteracted by the viscous friction force, as described by Stokes' formula. Incorporating specific force terms into the Langevin equation allows for the investigation of diverse and complex BM scenarios across various domains. Examples include BM coupled with a magnetic field [12], BM influenced by laser-induced temperature field [13], and BM subjected to electric fields [14]. Furthermore, the discourse on Brownian motion extends to the realm of anisotropic droplets, where researchers often employ an orientation-dependent Langevin model [15,16]. Expanding the scope, the inclusion of hydrodynamic memory effects [17], which account for the inertial influence of the surrounding matrix on Brownian droplets, has led to the study of non-Markovian BM. This is accomplished by introducing a history-dependent Basset-Boussinesq-Oseen force term into

*fei.wang@kit.edu

the Langevin model [18]. Each of these instances adds distinctive features to the conventional Brownian motion model. The intricate interplay between complex fields and thermal fluctuations leads to an apparent transition in droplet dynamics. At short time intervals, these transitions manifest as a shift from Brownian behavior, with $\langle \Delta X^2 \rangle \sim t$, to ballistic behavior, with $\langle \Delta X^2 \rangle \sim t^2$, yet retaining Brownian behavior at longer timescales. Notably, the resultant motion closely resembles the self-propulsion observed in biological entities, such as E. coli bacteria and spermatozoa [19]. This is of paramount importance in comprehending the dynamics of active matter, a phenomenon often referred as active Brownian motion (ABM). Consequently, corresponding fluctuation-dissipation theorem (FDT) is also tailored to ABM, grounded in the principles of Langevin mechanics [20].

Confucius once espoused the wisdom of revisiting established theories to uncover new knowledge. In this research endeavor, we revisit the passive BM of submicrometer droplets and focus on the thermal composition noises. These noises emerge from the fluctuations in chemical free energy, a factor not typically considered in traditional Langevin mechanics. A notable scenario is reported in Ref. [21], cellular protein droplets exhibit pronounced composition noise [22], while demonstrating weak to moderate hydrodynamic effects due to the dynamic arrest of proteins [22,23]. Given the significance of protein molecule stability under thermal noise as well as the importance of Brownian motion-induced protein droplet coalescence [24] for live organisms, we have developed two distinct phase-field models. These models aim to explore the Brownian motion of tiny droplets in the presence of intense composition noise coupled with varying degrees of hydrodynamics.

In our model, we establish an equivalence between Langevin mechanics and the Navier-Stokes equation to consider the fluid dynamics, as outlined in Ref. [25]. To account for the crucial role of composition noise in tiny droplets, we introduce the stochastic phase-field equation, which imparts substantial significance to random behaviors. While the composition fluctuations is predominantly dissipated by diffusion, it remains intricately linked to the strong surface tension effect which converts perturbations in chemical free energy into fluctuations in kinetic energy and results in the so-called Marangoni flow. This transformative mechanism falls beyond the purview of the conventional fluctuation-dissipation theorem and Langevin mechanics. Furthermore, employing a multicomponent multiphase model, we explore the interactions of multiple droplets, incorporating the interplay of diffusion, surface tension-induced Marangoni effects, and viscous friction. The inclusion of composition noise not only introduces a new degree of freedom to equilibrium Brownian motion but also precipitates various nonequilibrium behaviors.

This paper is structured as follows: in Sec. II, two mathematical models are presented. The numerical stability of the model discretization is validated with the capillary-wave theory in Sec. III. In Sec. IV A, we study the equilibrium of the droplet motion with both models, where the Einstein's theory $D^* \sim k_B T/r_0$ is recovered. In Sec. IV B, we show two nonequilibrium behaviors stemming from the thermal noise. First, the single droplet motion transforms from Brownian to Ballistic which indicates a distinct energy dissipation mechanism from FDT. Second, the multidroplet simulation shows an underlying coalescence mechanism that is generated by the noise-induced nonuniform velocity field. A comparison with previous Golovin-Tanaka coalescence mechanism is made; differences from previous work are discussed.

II. NUMERICAL MODEL

A. Stochastic Allen-Cahn-Navier-Stokes model

We consider a system consisting of N Brownian droplets ($N \in \mathbb{Z}$) in a domain Ω. The Brownian droplets are characterized by a vector of phase order parameters $\boldsymbol{\phi}(\boldsymbol{x}, t)$ in the Gibbs simplex $G = \{\boldsymbol{\phi} \in \mathbb{R}^{N+1} : \sum_{\alpha=0}^{N} \phi_\alpha = 1,\ \phi_\alpha \geqslant 0\}$. The index 0 is especially assigned for the matrix with $\phi_0 := \phi_M$. The chemical free-energy functional $\mathcal{F}$ of the system is written as a function of the order parameter as

$$\mathcal{F} = \int_\Omega \left[g(\boldsymbol{\phi}) + \epsilon\, a(\boldsymbol{\phi}, \nabla\boldsymbol{\phi}) + \frac{\omega(\boldsymbol{\phi})}{\epsilon} \right] d\Omega. \tag{2}$$

Here, ϵ is a parameter related to the interface width. The bulk chemical free-energy density is defined by $g(\boldsymbol{\phi})$, which is used to ensure volume conservation acting as the role of a Lagrangian multiplier. Similar to the work of Landau [26], the gradient energy density $a(\boldsymbol{\phi}, \nabla\boldsymbol{\phi})$ is formulated by a generalized asymmetric expression as [27]

$$a(\boldsymbol{\phi}, \nabla\boldsymbol{\phi}) = \sum_{\alpha<\beta}^{N,N} \gamma_{\alpha\beta} (\phi_\alpha \nabla\phi_\beta - \nabla\phi_\alpha \phi_\beta)^2, \tag{3}$$

where $\gamma_{\alpha\beta}$ denotes the interfacial tension between α and β phases. The last chemical free-energy contribution $\omega(\boldsymbol{\phi})$ is formulated as a nonconvex function with $N+1$ global minima, which characterize the equilibrium states of the N droplets and the matrix. To save computational effort, we adopt a multi-obstacle potential [28–30] as

$$\omega(\boldsymbol{\phi}) = \begin{cases} \frac{16}{\pi^2} \sum_{\alpha<\beta}^{N,N} \gamma_{\alpha\beta} \phi_\alpha \phi_\beta + \sum_{\alpha<\beta<\gamma}^{N,N,N} \chi^* \phi_\alpha \phi_\beta \phi_\gamma, & \text{if } \boldsymbol{\phi} \text{ in } G \\ +\infty, & \text{else.} \end{cases} \tag{4}$$

Here, the penalty parameter χ^* models the triple interactions in the system and avoids the occurrence of the third component contribution at two droplet interfaces. Physically, the choice of χ^* affects the evolution of the energy landscape from the bulk of one droplet to another bulk following the gradient descent trajectory; the value of χ^* reflects the triple molecular interaction in a lattice model and should be determined by the phase diagram. More details about the obstacle potential is documented in the Supplemental Material, Sec. I.1 [31].

Under the assumption of incompressibility, the evolution of the phase-field variable $\boldsymbol{\phi}$ and the fluid velocity $\boldsymbol{u}$ in the system is controlled by the Allen-Cahn-Navier-Stokes (ACNS) equations [32] as

$$\nabla \cdot \boldsymbol{u} = 0, \tag{5}$$

$$(\partial_t \boldsymbol{\phi} + \boldsymbol{u} \cdot \nabla\boldsymbol{\phi}) = -\frac{1}{Pe}(\tau \boldsymbol{\mu}_\phi + \sqrt{\tau}\, \boldsymbol{\xi}_\phi + \lambda), \tag{6}$$

$$\rho\, (\partial_t \boldsymbol{u} + \boldsymbol{u} \cdot \nabla\boldsymbol{u}) = \frac{-\nabla P - \boldsymbol{\phi}\nabla\boldsymbol{\mu}_\phi}{\mathrm{We}} + \frac{\eta \nabla^2 \boldsymbol{u}}{\mathrm{Re}} + \frac{\sqrt{\eta}\, \boldsymbol{F}}{\mathrm{Re}}. \tag{7}$$

The kinetic parameter τ controls the evolution rate of $\boldsymbol{\phi}$ towards equilibrium. The chemical potential $\boldsymbol{\mu}_\phi$ is defined as $\delta\mathcal{F}/\delta\boldsymbol{\phi}$. The Lagrange multiplier λ ensures the constraint $\sum_{\alpha=0}^{N}\phi_\alpha = 1$ by taking the following formulation:

$$\lambda = \frac{1}{N+1}\sum_{\alpha=1}^{N+1}\left(\tau\,\mu_{\phi\alpha} + \sqrt{\tau}\,\xi_{\phi\alpha}\right). \tag{8}$$

The pressure is labeled P. The density ρ and the dynamic viscosity η are linearly interpolated over the individual densities and viscosities of each droplet and matrix as $\rho = \sum_{\alpha=0}^{N}\rho_\alpha\phi_\alpha$ and $\eta = \sum_{\alpha=0}^{N}\eta_\alpha\phi_\alpha$, respectively. In the discussion section on the ACNS model, the subscripts $_P$ and $_M$ stand for the proprieties of the droplet and the matrix, respectively. Without losing generality, the density and the viscosity of the matrix are set as the reference value to vary the corresponding values of the droplets in the current work. The dimensionless quantities Pe, Re, and We are calculated by the characteristic velocity u^*, diffusivity D^*, length x^*, density ρ^*, viscosity η^*, and surface tension σ^* as

$$\mathrm{Pe} = \frac{u^*x^*}{D^*}, \quad \mathrm{Re} = \frac{\rho^*u^*x^*}{\eta^*}, \quad \mathrm{We} = \frac{\rho^*u^{*2}x^*}{\sigma^*}.$$

In this work, we set $\mathrm{Re} = 1.0$, $\mathrm{Pe} = 1.0$, and $\mathrm{We} = 100$, if not specified differently.

Noteworthily, two types of stochastic processes are coupled in the ACNS model, namely, (a) the composition fluctuation $\boldsymbol{\xi}_\phi = (\xi_{\phi_0}, \xi_{\phi_2}, \ldots, \xi_{\phi_N}) = (\xi_\phi, \xi_\phi, \ldots, \xi_\phi)$, and (b) the random body force term $\boldsymbol{F}$. Both noises are Gaussian and spatially and temporally relevant as

$$\langle\xi_\phi, \xi'_\phi\rangle = \frac{2\,k_BT}{v_l\,\Delta t}\delta(\boldsymbol{x}-\boldsymbol{x}')\delta(t-t'), \tag{9}$$

$$\langle\boldsymbol{F}, \boldsymbol{F}'\rangle = \frac{2\,k_BT}{v_l\,\Delta t}\nabla^2\delta(\boldsymbol{x}-\boldsymbol{x}')\delta(t-t'). \tag{10}$$

According to the fluctuation-dissipation theorem (FDT), the noise amplitudes are decided by the Boltzmann constant k_B, the temperature T, the lattice volume v_l, and the simulation time step Δt.

B. Stochastic Cahn-Hilliard-Navier-Stokes model

We postulate another conserved Cahn-Hilliard-Navier-Stokes model to characterize Brownian droplets in a domain Ω by its composition $c(\boldsymbol{x}, t)$, while the matrix composition is $1 - c(\boldsymbol{x}, t)$. The chemical free-energy functional $\mathcal{F}$ of the system is then written as

$$\mathcal{F} = \int_\Omega [f(c) + \sigma\epsilon(\nabla c)^2]d\Omega. \tag{11}$$

Here, the liquid-matrix interfacial tension γ is determined by the surface tension parameter σ [33]. The parameter ϵ is related to the interface width. The bulk chemical free-energy density $f(c)$ takes the regular solution formulation as [34]

$$f = \frac{R_gT}{v_m}[c\ln c + (1-c)\ln(1-c)] + \chi\,c\,(1-c), \tag{12}$$

where R_g denotes the universal gas constant, and v_m represents the molar volume. The molecular interaction between droplet and matrix is scaled by the Flory parameter χ which takes 3.78 for the system with an upper critical-point phase diagram in this work. More details about the free-energy formulation Eq. (12) and a comparison with the obstacle potential adopted in Allen-Cahn model is documented in supplementary Sec. I.2 [31]. Under the assumption of incompressibility, the evolution of the Brownian droplet composition c and the fluid velocity $\boldsymbol{u}$ in the system is governed by the stochastic Cahn-Hilliard-Navier-Stokes (CHNS) equations [32] as

$$\nabla\cdot\boldsymbol{u} = 0,$$

$$\partial_t c + \boldsymbol{u}\cdot\nabla c = \frac{\nabla}{\mathrm{Pe}}\cdot(\mathcal{M}\nabla\mu + \sqrt{\mathcal{M}}\,\boldsymbol{\xi}_c), \tag{13}$$

$$\rho\,(\partial_t\boldsymbol{u} + \boldsymbol{u}\cdot\nabla\boldsymbol{u}) = \frac{-\nabla P - c\nabla\mu}{\mathrm{We}} + \frac{\eta\nabla^2\boldsymbol{u}}{\mathrm{Re}} + \frac{\sqrt{\eta}\,\boldsymbol{F}}{\mathrm{Re}}. \tag{14}$$

Here, the chemical potential $\mu = \delta\mathcal{F}/\delta c = \partial f/\partial c - 2\sigma\epsilon\nabla^2 c$ is magnified by the mobility $\mathcal{M}$, which propels the diffusion. The mobility takes Onsager's relation as $\mathcal{M} = \mathcal{M}_0 c(1-c)$ with $\mathcal{M}_0 = (\epsilon/\sigma)[D_P(1-c) + D_M c]$. D_P and D_M stand for the self-diffusivity of the droplet and matrix, respectively [35]. The surface tension force $-c\,\nabla\mu$ induces the convection and the pressure term P is solved by the Poisson equation resulting from the incompressible flow. The density ρ and the dynamic viscosity η are linearly interpolated as $\rho(c) = (\rho_1 - \rho_2)c + \rho_2$, $\eta = (\eta_1 - \eta_2)c + \eta_2$. At the droplet (matrix) equilibrium composition c_0 (c_1), we have $\rho(c_0) = \rho_P$, $\eta(c_0) = \eta_P$ [$\rho(c_1) = \rho_M$, $\eta(c_1) = \eta_M$]. Like the previous ACNS model, two types of stochastic processes are coupled in the CHNS model, namely, (i) the composition fluctuation flux term $\boldsymbol{\xi}_c$ as

$$\boldsymbol{\xi}_c = \begin{cases} (\xi_x) = (\xi_c), & \text{for one dimension} \\ (\xi_x, \xi_y) = (\xi_c, \xi_c), & \text{for two dimensions} \\ (\xi_x, \xi_y, \xi_z) = (\xi_c, \xi_c, \xi_c), & \text{for three dimensions,} \end{cases}$$

whose component is Gaussian and spatially and temporally relevant as

$$\langle\xi_c, \xi'_c\rangle = \frac{2\,k_BT}{v_l\,\Delta t}\nabla^2\delta(\boldsymbol{x}-\boldsymbol{x}')\delta(t-t'). \tag{15}$$

For example, the composition noise amplitude of pure water at 298.15 K takes 0.203 after nondimensionalization (see the Supplemental Material [31]). (ii) $\boldsymbol{F}$ is identical to Eq. (10) of the ACNS model.

C. Simulation setup and boundary conditions

The finite difference method is implemented on a staggered mesh with a size of $Nx \times Ny \times Nz$ and equidistant Cartesian spacing $\Delta x = \Delta y = \Delta z$ to solve the evolution equations, namely, the Allen-Cahn equation (6) and the Cahn-Hilliard equation (13). The Navier-Stokes equations (7) and (14) are updated with the explicit Euler scheme, the phase-field variables $\boldsymbol{\phi}$, the concentration c, and the fluid velocity $\boldsymbol{u}$ are subjected to the periodic boundary conditions. The discretized space and time steps are shown in Table SI in the Supplemental Material [31]. Parallelization of the numerical algorithm is achieved with message passing interface (MPI) techniques. The numerical convergence of the model is demonstrated in the next section. The simulations are performed on the parallel computer bwUniCluster of Baden-Württemberg equipped with Intel Xeon Gold CPUs in the environment of Red Hat Enterprise.

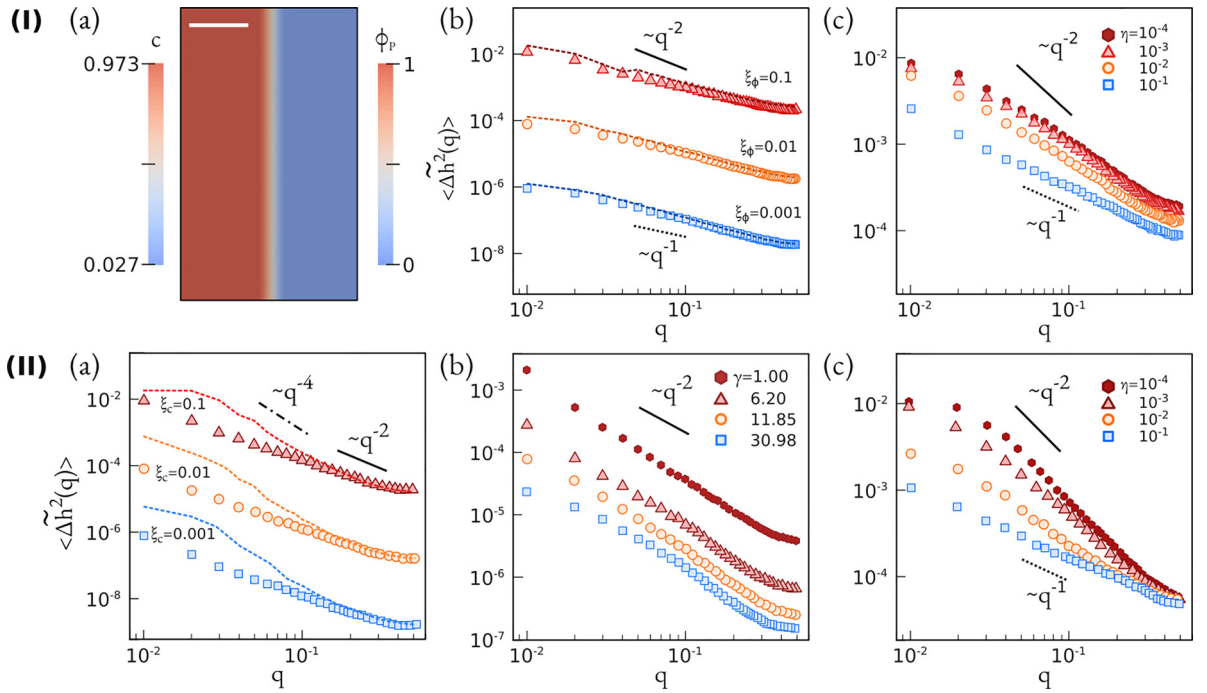

FIG. 1. Validation of the two stochastic phase-field models with the capillary-wave theory. Open colored symbols: with hydrodynamics; dashed color lines: without hydrodynamics. (I) Allen-Cahn-Navier-Stokes model: (a) The initial unperturbed flat interface. (b) The capillary-wave amplitudes $\langle\Delta\widetilde{h}^2(q)\rangle$ according to Eq. (17) in the reciprocal space for the perturbed interface with different composition noise amplitudes ξ_ϕ. (c) $\langle\Delta\widetilde{h}^2(q)\rangle$ with distinct viscosities η, for a fixed value of noise amplitude, $\xi_\phi = 0.1$. (II) Cahn-Hilliard-Navier-Stokes model: (a) The capillary-wave amplitudes increasing with $\boldsymbol{\xi}_c$. (b) $\langle\Delta\widetilde{h}^2(q)\rangle$ versus q for different interfacial tensions, γ at noise amplitude $\boldsymbol{\xi}_c = 0.05$. (c) $\langle\Delta\widetilde{h}^2(q)\rangle$ versus q for different viscosities η with noise amplitude $\boldsymbol{\xi}_c = 0.1$. The black solid lines guide the capillary-wave theory relationship of $\langle\Delta\widetilde{h}^2(q)\rangle \sim q^{-2}$. The dotted, solid, and dot-dashed lines show different scaling laws, $\langle\Delta\widetilde{h}^2(q)\rangle \sim q^{-1}$, $\sim q^{-2}$, and $\sim q^{-4}$, respectively.

III. VALIDATION

A. Capillary-wave theory

For liquid surfaces with small thermal noise, the capillary-wave theory (CWT) is regarded as a decent way to describe its behavior which has been proven by several experiments [36,37] and simulations [38]. Perturbed by the noise, the surface energy increase ΔE of a planar fluid interface is proportional to the surface area change as

$$\Delta E \approx \frac{\gamma}{2}\int (\nabla h)^2\, dxdy, \tag{16}$$

where the interface position h is defined by the location with composition $\phi_P = 0.5$ for ACNS, and $c = 0.5$ for the CHNS model. The liquid-matrix interfacial tension is represented by γ. After Fourier transformation, Eq. (16) is expressed in the reciprocal space as

$$\Delta E(q) = \frac{\gamma}{2}\int q^2|\Delta\widetilde{h}(q)|^2 dq,$$

where q symbolizes the wave number, and $\widetilde{h}(q)$ represents the capillary-wave amplitude in the wave number domain. In statistical mechanics, each wave mode of the fluctuation has the identical energy k_BT, so that

$$\langle\Delta\widetilde{h}^2(q)\rangle = \frac{k_BT}{4\pi^2q^2\gamma}, \text{ with } \gamma \sim \chi, \tag{17}$$

where $\langle\Delta\widetilde{h}^2(q)\rangle$ is named as the structure factor of the fluid interface. According to the noise formulations stated by Eqs. (9) and (15), we have $\langle\Delta\widetilde{h}^2(q)\rangle \propto \xi_\phi^2$ and $\langle\Delta\widetilde{h}^2(q)\rangle \propto \xi_c^2$ for ACNS and CHNS, respectively.

To validate the energy dissipation behaviors of the ACNS and CHNS models with the capillary-wave theory (CWT), an initial setup with a flat liquid-matrix interface is demonstrated in Fig. 1(I)(a). The density $\rho = 0.01$ and the interfacial tension $\gamma = 1.0$ are adopted for both models. First, for the ACNS model, two scenarios, namely, (i) the Allen-Cahn model with hydrodynamics (open dots) and (ii) without hydrodynamics (dashed lines) are considered and shown in Fig. 1. The phase-field kinetic parameter τ in the ACNS model is set to be 0.01 and the viscosity is $\eta = 0.001$. Figure 1(I)(b) shows the squared capillary-wave amplitude $\langle\Delta\widetilde{h}^2(q)\rangle$ with the wave number q for different composition noise amplitudes ξ_ϕ. The scaling law with $q^{-1} < \langle\Delta\widetilde{h}^2(q)\rangle < q^{-2}$ appears in both scenarios irrespective of hydrodynamics, as guided by the black lines. With the growth of the noise amplitude ξ_ϕ by 10 times, $\langle\Delta\widetilde{h}^2(q)\rangle$ increases accordingly by 10^2 times, showing good consistence with Eq. (17). Figure 1(I)(c) illustrates the impact of the viscosity $\eta = \eta_P = \eta_M$ on $\langle\Delta\widetilde{h}^2(q)\rangle$ at a fixed noise amplitude $\xi_\phi = 0.1$. Not only the capillary-wave amplitude decreases with larger viscosity, but the scaling factor reduces to -1 at large viscosity. This scaling law does not obey CWT, implying that the stochastic ACNS model embodies a distinct energy dissipation mechanism for the perturbed interface from the binary fluid systems.

Next, the CHNS model is validated and the results are shown in Fig. 1(II). Here, the structure factor $\langle\Delta\widetilde{h}^2(q)\rangle$ is also measured for two scenarios: (i) with hydrodynamics (open

dots) and (ii) without hydrodynamics (dashed lines). The mobility $\mathcal{M}_0$ set to be 1.0 and the viscosity is $\eta = 0.001$. In good consistency with previous researches [37], at large wave number q, $\langle \Delta\widetilde{h}^2(q)\rangle$ shows the q^{-2} tendency with the wave number q for both scenarios, as guided by the black solid line in Fig. 1(II)(a). For the short wavelength perturbations with $q < 0.1$, the Cahn-Hilliard model without hydrodynamics (dashed colored lines) shows an apparent deviation from the CWT scaling law. It indicates that hydrodynamics is a crucial mechanism for the surface energy dissipation of the fluid interface, especially for the noise with short wavelengths. Then, in Fig. 1(II)(b), we fix the constant noise amplitude $\xi_c = 0.05$ and observe the reduction in capillary-wave amplitudes with the increase in the surface tension γ which is in good accordance with the CWT. In Fig. 1(II)(c), the viscosity effect on the scaling law of $\langle \Delta\widetilde{h}^2(q)\rangle$ versus q is illustrated. By setting a larger η, the viscous stress $\eta\nabla^2\boldsymbol{u}$ in the Navier-Stokes equation is magnified, giving rise to a stronger energy dissipation via frictional forces between fluids. But the deduction of Eq. (17) only considers the surface energy dissipation and does not take the viscosity effect on the kinetic energy into account. This observation in turn indicates that for the composition noise dominated Brownian motion of submicro droplets, the viscous effect is of subtle importance. In this way, we set low viscosity $\eta = 0.001$ in the following parts to eliminate the viscous dissipation mechanism, which is in line with the CWT and experiments.

B. Dispersion relation

To have a better understanding of the capillary-wave theory for two types of phase-field models, we scrutinize the energy dissipation by the dispersion relation which explains the distinct scaling laws between the capillary-wave amplitude $\langle \Delta^2 h\rangle$ with the wave number q. Here, we suggest two regimes with distinct dispersion relations, namely, composition noise dominated regime and convection dominated regime.

1. Composition noise dominated regime

(I) For the ACNS model, the thermal fluctuation energy-gaining rate of the system reads

$$\frac{\partial \mathcal{F}^+}{\partial t} = \int_\Omega f^* \tau\, \xi_\phi^2\, d\Omega = f^* \tau_0\, \xi_\phi^2\, \mathrm{S},$$

where S is the interface area and the characteristic energy density $f^* = \gamma/\epsilon$. The energy dissipation rate by the diffusion process obeys the following energy law as

$$\begin{aligned}\frac{\partial \mathcal{F}^-}{\partial t} &= \int_\Omega \frac{\delta F}{\delta \phi}\frac{d\phi}{dt} d\Omega = -\int_\Omega \tau\, \mu^2 d\Omega \\ &= -\int_\Omega \tau[\gamma(1-2\phi) - \gamma\nabla^2\phi]^2 d\Omega \\ &= \mathrm{S}\int_{-\infty}^{\infty} \bar{\alpha}\, \tau\, f^{*2}\,(1 + 2\pi^2\epsilon^2 q^2 + \pi^4\epsilon^4 q^4)\bar{\phi}^2 dx \\ &= \bar{\alpha}\, \tau_0\, f^{*2}\, \mathrm{S}\,(1 + 2\pi^2\epsilon^2 q^2 + \pi^4\epsilon^4 q^4)\Delta^2 h.\end{aligned}$$

Here, we expand the composition at the interface location $\phi = 0.5$ to the first order of infinitesimal length $\bar{\epsilon}$ and integrate by substituting $\phi = 0.5 + \bar{\epsilon}\,\bar{\phi}$. With tiny thermal noises, the composition perturbation $\bar{\phi}$ is described by a wave function $e^{\xi t - iqy}$. Therefore, the terms $\nabla\bar{\phi}$ and $\nabla^2\bar{\phi}$ are linearized as $-i\,q\,\bar{\phi}$ and $q^2\,\bar{\phi}$, respectively. In addition, we rewrite $\bar{\phi} = \Delta\phi = \nabla\phi\cdot\Delta h$ and let $\bar{\alpha} = 16\,\bar{\epsilon}^2/\pi^4$. Moreover, the first-order approximation simplifies $\int_{-\infty}^{\infty}(\nabla\phi)^2 dx$ by the Dirac δ function. In this way, at equilibrium, we have $\partial_t F^+ = \partial_t F^-$ which denotes the balance between energy gaining and consumption, so that

$$\Delta^2 h \propto \frac{\xi_\phi^2}{\gamma\,(1 + 2\pi^2\epsilon^2 q^2 + \pi^4\epsilon^4 q^4)}. \tag{18}$$

With this dispersion relation, we address the scaling law of the capillary-wave amplitudes observed in Fig. 1(I). Distinct from the Fick's second law and the Cahn-Hilliard equation, the Allen-Cahn equation is a diffusion-reaction equation and can be expressed with the composition perturbation $\bar{\phi}$ as

$$\frac{d\bar{\phi}}{dt} = \tau\left(\frac{16\gamma}{\pi^2\epsilon}\bar{\phi} - \gamma\epsilon\,\nabla^2\bar{\phi}\right).$$

For small-wavelength noises, the linear term of $\bar{\phi}$ controls the energy dissipation over the curvature-related $\nabla^2\bar{\phi}$ term. While for the long-wavelength perturbations, the second-order term comes into play, resulting the scaling factor of $\langle\Delta^2 h\rangle$ approaching -2.

(II) For the CHNS model, the fluctuation energy-gaining rate reads

$$\frac{\partial \mathcal{F}^+}{\partial t} = \int_\Omega f^* \mathcal{M}\,\xi_c^2\, d\Omega = f^*\mathcal{M}_0\,\xi_c^2\,\mathrm{S}.$$

Meanwhile, the energy dissipates as

$$\begin{aligned}\frac{\partial \mathcal{F}^-}{\partial t} &= \int_\Omega \frac{\delta F}{\delta c}\frac{dc}{dt} d\Omega \\ &= -\int_\Omega \mathcal{M}(\nabla\mu)^2 d\Omega \\ &= \mathrm{S}\int_{-\infty}^{\infty} \mathcal{M}\, f^{*2}\,\bar{\epsilon}^2\,(q^2\chi^2 + 2\epsilon^2 q^4\chi + \epsilon^4 q^6)\,\bar{c}^2\, dx \\ &= \mathcal{M}_0\, f^{*2}\,\bar{\epsilon}^2\,\mathrm{S}\,(q^2\chi^2 + 2\epsilon^2 q^4\chi + \epsilon^4 q^6)\Delta^2 h,\end{aligned}$$

in which the integrated term is expanded at the interface position with $c = 0.5 + \bar{\epsilon}\,\bar{c}$. Similar to the mathematical treatments in the ACNS model, the composition perturbation $\bar{c}$ is analogized with the wave function $e^{\xi t - iqy}$. At equilibrium, we obtain

$$\Delta^2 h \propto \frac{\xi_c^2}{\gamma\,(\chi^2 q^2 + 2\chi\,\epsilon^2 q^4 + \epsilon^4 q^6)}. \tag{19}$$

Both q^{-2} and q^{-4} scaling laws are captured in the simulated CWT of the Cahn-Hilliard model without hydrodynamics; see dashed lines in Fig. 1(II)(a). It reflects the prominent difference between the Cahn-Hilliard equation and the diffusion equation (Fick's second law), since CH is a fourth-order partial differential equation expressed with composition perturbation $\bar{c}$ as

$$\frac{d\bar{c}}{dt} = \nabla\cdot\left(\mathcal{M}\frac{\sigma\chi}{\epsilon}\nabla\bar{c}\right) - \nabla\cdot(\mathcal{M}\sigma\epsilon\,\nabla^3\bar{c}).$$

Hence, the energy dissipation for small-wavelength noises (large q) behaves similarly to the standard diffusion process. While for the large wavelength (small q), its dissipation is dominated by the fourth-order term $\sigma\nabla^4\bar{c}$.

2. Convection dominated regime

The energy law behaves entirely differently when convection overwhelms diffusion, and we have another energy law for the ACNS model:

$$\begin{aligned}\frac{\partial \mathcal{F}^-}{\partial t} &= \int_\Omega \boldsymbol{u}\cdot\rho\frac{d\boldsymbol{u}}{dt}\,d\Omega = \int_\Omega \boldsymbol{u}\cdot(\mu\nabla c)\,d\Omega \\ &= \mathrm{S}\int_{-\infty}^{\infty}\nabla\Psi\cdot\frac{16f^*}{\pi^2}(-\bar{\epsilon}\,\bar{\phi}-\pi^2\epsilon^2\,\bar{\epsilon}\,\nabla^2\bar{\phi})(\bar{\epsilon}\,\nabla\bar{\phi})dx \\ &= \frac{16f^*\,\mathrm{S}}{\pi^2}\bar{\epsilon}^{\,2}q'\Psi\,(\chi\,q+\pi^2\epsilon^2q^3)\Delta^2h.\end{aligned}$$

Here, we assume the velocity $\boldsymbol{u}$ as the gradient of the tiny perturbed stream function $\Psi = e^{\zeta' t - iq' x}$ with the different phase parameter q' from the composition noise. Under this circumstance, the capillary-wave amplitude is derived as follows:

$$\Delta^2 h \propto \frac{\tau_0\,\xi_\phi^2}{q+\pi^2\,\epsilon^2\,q^3}. \tag{20}$$

Comparing with Eq. (18), $\langle\Delta^2 h\rangle$ has a scaling factor between -1 and -2 with respect to the wave number q in the ACNS model. Similarly, the energy law for the convection-dominated CHNS model is deduced as

$$\Delta^2 h \propto \frac{\mathcal{M}_0\,\xi_c^2}{\chi\,q+\epsilon^2\,q^3}, \tag{21}$$

which is also in line with the CWT simulation results shown in Fig. 1(II). These dispersion relations are dealing with the composition noise dissipated via convection, and has never been considered in previous FDT and CWT theories. We stress that this energy dissipation mechanism is entirely different from the one in the Langevin mechanics, where the random body force gets smoothed by the viscous stress. Testified in previous simulations [39,40], the random body force perturbed interface still follows the CWT scaling law with $\langle\Delta^2 h\rangle \sim q^{-2}$.

IV. RESULT AND DISCUSSION

In this section, we present the Brownian motion simulations with both models of CHNS and ACNS. Different noise amplitudes, droplet radius, and droplet-matrix interfacial tension are considered, and their impacts on Brownian behaviors are discussed.

A. Equilibrium behaviors

1. The Einstein's relation

We present a simple proof of the Einstein relation replicated with the phase-field model. The total fluctuation energy normalized by the characteristic chemical free-energy density f^* on the two-dimensional (2D) droplet with radius r_0 reads

$$\begin{aligned}\langle E\rangle/f^* &= \int_\Omega \langle\sqrt{\tau}\,\xi_\phi,\sqrt{\tau}\,\xi_\phi'\rangle\,d\Omega \\ &= \tau_0\,\xi_\phi^2\int_0^\infty \phi\,(1-\phi)\,2\pi r\,dr \\ &= \tau_0\,\xi_\phi^2\,\mathrm{S},\end{aligned}$$

where $\mathrm{S} = \int_0^\infty \phi\,(1-\phi)\,2\pi\,rdr = 2\pi r_0$ represents the surface area of the perfect spherical droplet with the interface width approaching the sharp interface limit [41]. The characteristic chemical free energy f^* equates to 1.0 after nondimensionalization. Consequently, with the property of the Rayleigh distribution, the root mean square droplet velocity in 2D reads

$$v_{rms} = \sqrt{\langle \boldsymbol{v}^2\rangle} = \sqrt{\frac{2\langle E\rangle}{m}} = \sqrt{\frac{4\,\tau_0\,\xi_\phi^2}{r_0}} = \sqrt{2D^*_{AC}},$$

from which the Brownian coefficient D^* of the ACNS model follows

$$D^*_{AC} = \frac{2\,\tau_0\,\xi_\phi^2}{r_0}. \tag{22}$$

With the same method, the Brownian coefficient with the CHNS model reads

$$D^*_{CH} = \frac{2\,\mathcal{M}_0\,\xi_c^2}{r_0}. \tag{23}$$

To testify the Einstein's relation, we perform 2D Brownian motion simulations with the ACNS model first. A droplet with an initial radius of $r_0 = 20$ is placed amid the domain with a size of $12r_0 \times 12r_0$ which can eliminate the influence of boundary on the droplet motion [42] (see the Supplemental Material [31]). With an increase in the noise amplitude ξ_ϕ, the Brownian coefficient D^* shows a parabolic relation with ξ_ϕ, as guided by the red dashed line in Fig. 2(I)(a). According to Eq. (9), the linear dependency of D^* on k_BT is confirmed. Here, D^* is fitted with the Rayleigh distribution based on the droplet velocity distributions for 10^6 time steps, as sketched in Fig. 2(II)(a). For stronger noise (or higher temperatures), the probability distribution function (PDF) of velocity becomes broad and shifts to the high-velocity side, indicating enhanced droplet motion by the composition noise.

Next, we alter the droplet radius r_0 for a constant noise amplitude $\xi_\phi = 0.001$. The inverse relationship of $D^* \sim 1/r_0$ is clearly demonstrated in the middle row of Fig. 2(I)(b), as guided by the red dashed line. By increasing the droplet radius, we observe that the peak of the velocity PDF moves to the low velocity in Fig. 2(II)(b). It implies that the Brownian droplet approaching its equilibrium is influenced by the size effect. Moreover, we observe another linear relationship between D^* and the kinetic parameter τ which is shown in the lower row of Fig. 2(I)(c). Compared with the 2D droplet trajectories in Fig. 2(III), the larger molecular mobility not only enhances the macroscopic diffusion of the whole Brownian droplet but also modifies the motion behavior, which is discussed later in Sec. IV B 1. In addition, Einstein's relation is replicated with the CHNS model. The initial droplet radius is 20 and the surface tension parameter is set to be $\gamma = 1.0$. The remaining hydrodynamic parameters in the Navier-Stokes equation are identical to the setup in the validation section Sec. III. The Brownian coefficient D^* is obtained by fitting the droplet velocity with the Rayleigh distribution. Figures 3(I)(a)–3(I)(c) present three relations with $D^* \propto \xi_c^2$, $D^* \propto 1/r_0$, and $D^* \propto \mathcal{M}_0$, respectively, for various noise amplitudes ξ_ϕ, radii r_0, and mobility parameter $\mathcal{M}_0$. Minor differences between ACNS and CHNS are attributed to the different fluctuation-dissipation scaling laws of CWT in Sec. III. The equilibrium composition distribution at the

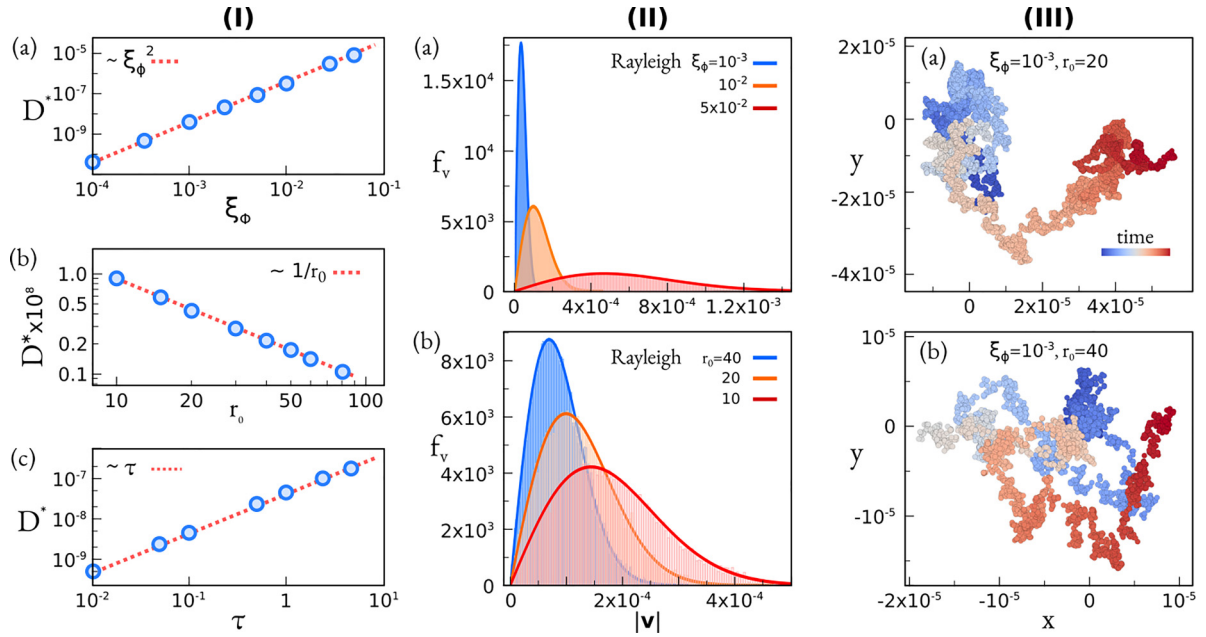

FIG. 2. 2D Brownian motion of droplets via ACNS model. (I) The Brownian motion coefficient D^* (a) with noise amplitude $\boldsymbol{\xi}_\phi$, (b) with initial radius r_0, (c) with kinetic parameter τ. The dashed red lines guide the $D^* \propto \xi_\phi^2$, $1/r_0$, and $1/\tau$ relations. (II) Probability density function (PDF) of droplet velocity follows the Rayleigh distribution (a) with $\boldsymbol{\xi}_\phi$, (b) with r_0. (III) The droplet trajectory. The color bar scales the time sequence.

interface for both models can also play a role, as sinus and hyper-tangent functions describe the ACNS and CHNS models, respectively. Therefore, the kinetic parameters τ and $\mathcal{M}$ are correspondingly assigned with different values, which results in the distinct spatial composition noises (scaled by $\sqrt{\tau}$ or $\sqrt{\mathcal{M}}$) at the interface region.

2. *Fluctuation-dissipation theorem*

Taking the CHNS model as an example, to trigger the Brownian motion, two thermal fluctuations are considered, namely, the composition noise $\sqrt{\mathcal{M}}\boldsymbol{\xi}_c$ and the random body force $\sqrt{\eta}\boldsymbol{F}$. Accordingly, each noise has its individual

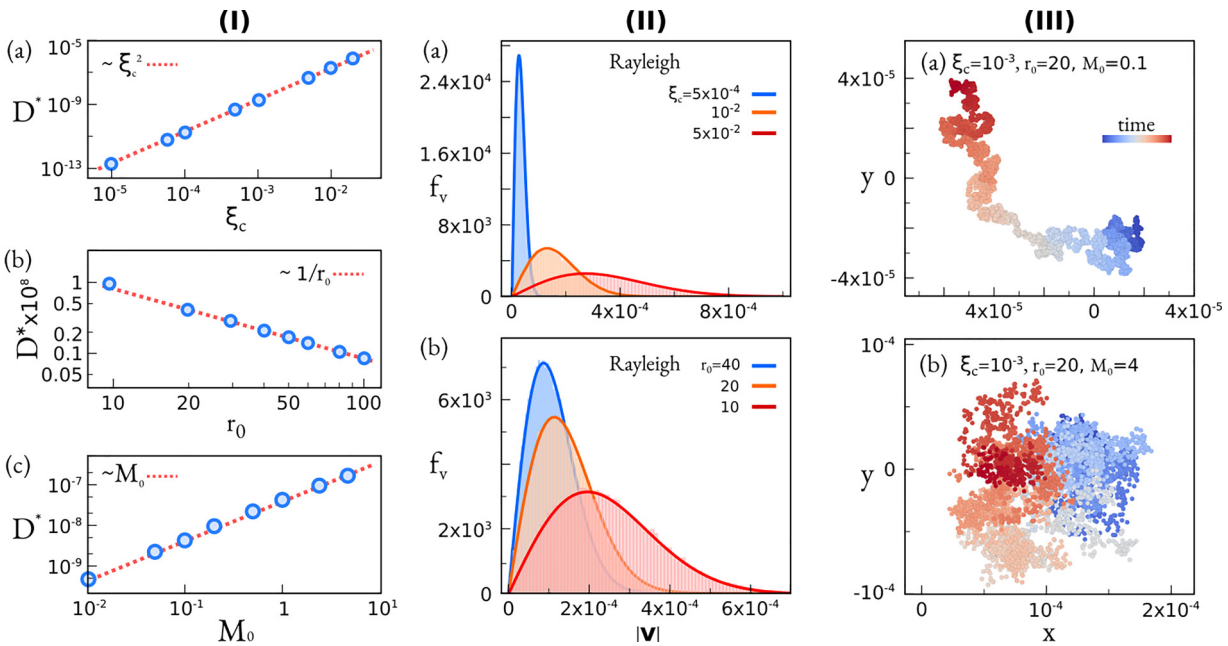

FIG. 3. 2D Brownian motion of droplets with CHNS model. (I) The Brownian motion coefficient D^* (a) with noise amplitude $\boldsymbol{\xi}_c$, (b) with initial radius r_0, (c) with mobility parameter $\mathcal{M}_0$. The dashed red lines guide the $D^* \propto \xi_\phi^2$, $1/r_0$, and $\mathcal{M}_0$ relations. (II) Probability density function (PDF) of droplet velocity follows the Rayleigh distribution (a) with $\boldsymbol{\xi}_c$, (b) with r_0. (III) The droplet trajectory. The color bar scales the time sequence.

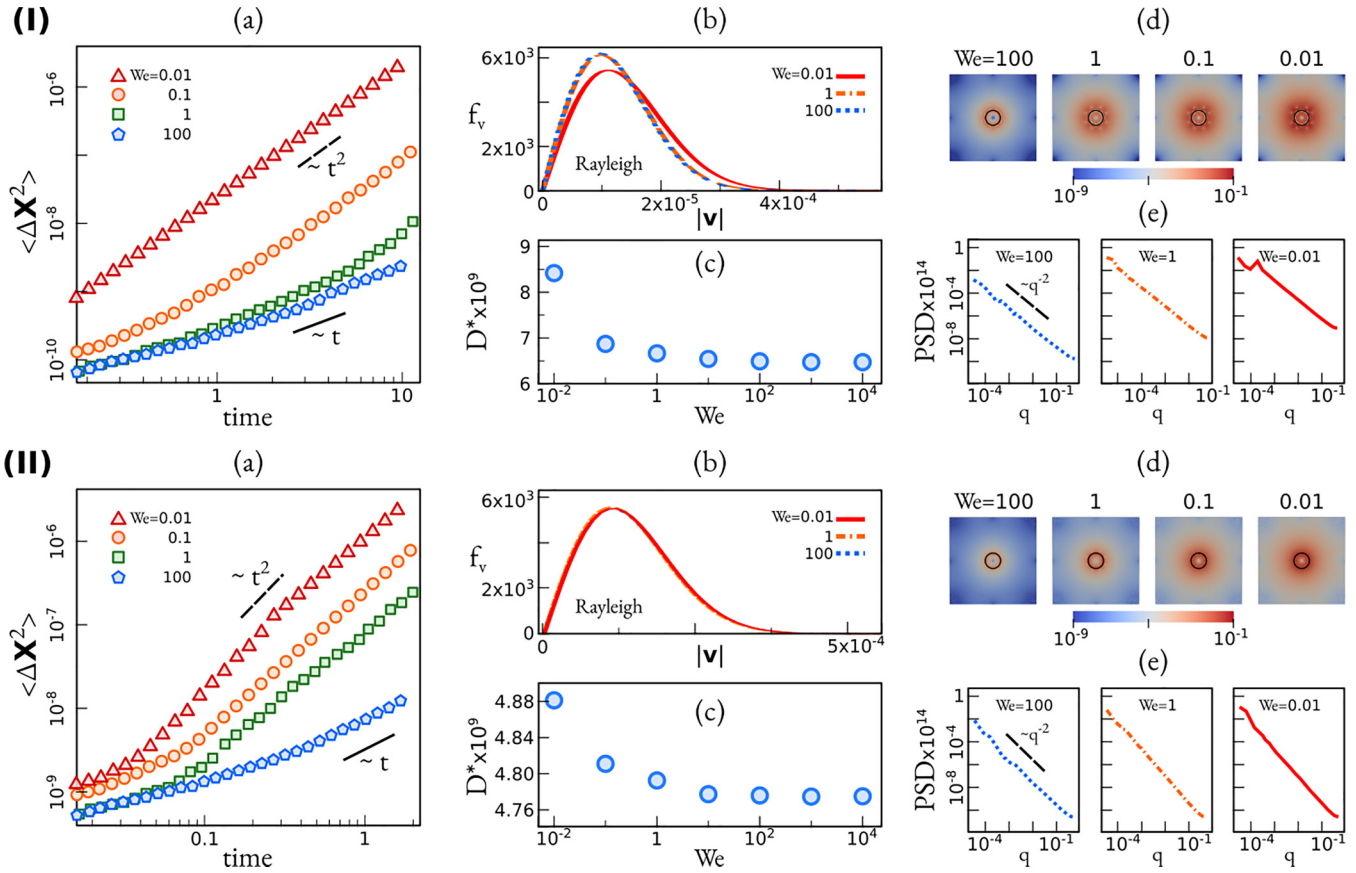

FIG. 4. 2D Brownian motion of a droplet for increasing hydrodynamics (Weber number We) with an initial radius $r_0 = 20$. (I) ACNS model with the composition noise amplitude $\xi_\phi = 0.001$: (a) Mean squared displacement with time. (b) Probability density function (PDF) of the velocity. (c) Brownian coefficient D^* with We. (d) Velocity field at $t = 200$. The black circles mark the droplet-matrix interface with $\phi = 0.5$. The color bar (log) scales the velocity magnitude. (e) Power spectral density (PSD) of the droplet displacement with the wave number q shows Brownian relationship PSD $\propto q^{-2}$. (II) CHNS model with the composition noise amplitude $\xi_c = 0.001$.

dissipation mechanism, as $\sqrt{\mathcal{M}}\,\boldsymbol{\xi}_c$ smoothed by diffusion and $\sqrt{\eta}\,\boldsymbol{F}$ by viscous friction. Hence, we categorize the BM into two subgroups, (I) the composition noise dominated BM which appears at higher temperatures and large intermolecular diffusivity, and (II) the random body force dominated BM for the rigid body. Each type has its individual Brownian coefficient as

$$D^* = \begin{cases} k_B T\ \zeta \propto \eta^{-1} & \text{for rigid body} \\ k_B T M \propto \mathcal{M}_0 & \text{for soft droplet.} \end{cases} \tag{24}$$

For the rigid body BM, the Brownian coefficient [43,44] follows the Stokes-Einstein-Sutherland relation where the hydrodynamic mobility $\zeta = (a\pi\,\eta\,r_0)^{-1}$ and the constant a is decided by the geometry of the motion. For the droplet BM in our simulation, the microscopic molecular mobility $\mathcal{M}$ scales the macroscopic droplet motion.

B. Nonequilibrium behaviors

The previous section addresses the equilibrium characteristics of the CHNS and ACNS models with which the Einstein's relation is reinstated, serving as a validation of our phase-field models and as an illustration of their ability to replicate thermodynamic equilibrium behavior. In the following section, we direct our focus to the nonequilibrium droplet behaviors that lie beyond the scope of thermodynamic equilibrium.

1. Marangoni effect and ballistic motion

In Einstein's derivation of the Brownian coefficient, the droplet is idealized as a rigid body, and the energy dissipation occurs primarily through the viscous stresses exerted by the surrounding matrix. In our model, we consider the surface tension effect of the submicro droplet, as its characteristic timescale is comparable with that of Brownian motion. Here, the composition-induced noise not only leads to inhomogeneous composition distributions at the interface region but also results in the interfacial tension gradients, invoking the surface tension force and the Marangoni flow [45] that drives the Brownian motion of the droplet. In our simulations, we manipulate the Weber number (We) to modulate the noise-induced surface tension force in the Navier-Stokes equations (7) and (14) for both ACNS and CHNS models. As demonstrated by the velocity field snapshots in Figs. 4(I)(c) and 4(II)(c), a reduction in We amplifies the surface tension force, enhancing the Marangoni flow around the droplets. Most importantly, the increasing Marangoni flow triggers a transition for the droplet motion from Brownian motion (associated with large We) to ballistic motion (associated with

small We). This transition is evident in the mean squared displacement (MSD) depicted in Figs. 4(I)(a) and 4(II)(a), where the ballistic behavior of $\langle \Delta \boldsymbol{X}^2 \rangle \sim t^2$ is illustrated by the dashed lines.

Notably, we propose that the ballistic behavior in droplet dynamics arises not from the fluctuation mechanism, but is rather related to the dissipation mechanism. One piece of evidence supporting this notion can be found by the droplet velocity distribution $f(\boldsymbol{v})$ in Figs. 4(I)(b) and 4(II)(b). We observe that an increase in Weber number exerts only minimal influence on $f(\boldsymbol{v})$. The reduction of We from 100 to 0.01 only leads to an increase of D^* by 5%. However, the droplet MSD follows a fundamentally different scaling law with time. Another piece of evidence is supported by the power spectral density (PSD) of the droplet displacement [46], which exhibits a -2 scaling law with wave number q in Figs. 4(I)(d) and 4(II)(d). Both observations signify that the ballistic droplet motion stems from the same origin with the Brownian motion—composition Gaussian noise.

In this way, we suggest that the ballistic dynamic is originated from the dissipation mechanism of the noise-induced surface tension force (which is also a kind of noise), that is not compatible with the conventional FDT stated in Sec. IV A 2. For standard FDT description, the composition perturbation $\sqrt{\mathcal{M}}\,\xi_c$ emanated from the chemical free-energy fluctuation is dissipated by the diffusion term $\mathcal{M}\nabla^2\mu$, and the random body force $\sqrt{\eta}\,\mathbf{F}$ arising from the kinetic energy gets smoothed out by the viscous term $\eta\nabla^2\mathbf{u}$. In this context, both noises are assumed to be independent with no covariance. However, in fact, not all of the chemical free-energy fluctuation is smoothed by diffusion. Parts of it are transformed into kinetic-energy perturbation by the Kortweg-stress associated surface tension force $-c\nabla\mu$ and induces the random Marangoni flow. This fluid flow can either be dissipated by the viscous stress, or in return transforms into the composition gradient. Hence, a more complex dynamics comes into play where the dissipation of the random Marangoni flow has the characteristic timescale determined by three aspects: (i) Péclet number Pe decides the amount of the chemical free-energy fluctuation transforming into the kinetic-energy perturbations; (ii) Weber number We scales the strength of Marangoni effect; (iii) Reynolds number, Re determines the viscous dissipation magnitude.

Consequently, for large composition noise dominated scenarios with low viscous fluids, the viscous dissipation is incapable of smoothing the random surface tension force in its characteristic timescale, resulting in the ballistic droplet motion. This scenario is reminiscent of the underdamped Langevin mechanics, especially in the genre of active Brownian motion, where the self-propelling active droplet also performs the ballistic motion with $\langle \Delta \boldsymbol{X}^2 \rangle \sim t^2$ [47]. But the differences between our observation and ABM are apparent. (i) The Marangoni flow only stems from the composition fluctuation, rather than from the inhomogeneous surfactant distributed around droplet [48]; (ii) the droplet motion is dissipated not only by the viscous friction, but also by the diffusion, because of the interconversion of chemical free energy and kinetic energy by the surface tension force.

2. Phase diagram of droplet motion

Upon thorough examination of droplet motion behaviors across various Pe and We values, we categorize droplet motion into three distinct scenarios characterized by trajectory and MSD.

(I) Brownian motion with subdiffusive drift: the mean squared displacement $\langle \Delta \boldsymbol{X}^2 \rangle < 2D^*t$. In this scenario, weak composition fluctuations are dissipated via intermolecular diffusion, while convection effects can be neglected. This scenario corresponds to the dark-blue region in the motion phase diagram of Figs. 5(I)(a) and 5(II)(a) and is prominent in cases with a large Peclet number and a high Weber number. The MSD shown by the blue pentagons in Figs. 5(I)(b) and 5(II)(b) from our simulations indicates a subdiffusive tendency in the MSD, deviating from the $\langle \Delta \boldsymbol{X}^2 \rangle \sim t$ behavior indicated by the solid line. Concurrently, the fourth cumulant $\langle \Delta \boldsymbol{X}^4 \rangle$ remains approximately at 10^{-32} without exhibiting any time dependence, implying that the droplet displacement adheres to a standard Gaussian distribution.

(II) Brownian motion with diffusive drift: convection becomes a significant factor. This scenario, characterized by a small Pe number and a large Weber number, is depicted by the light-blue regions in the motion phase diagram illustrated in Fig. 5. The composition noise, only partially dissipated through intermolecular diffusion, amplifies as Pe decreases, inducing the Marangoni flow that propels the droplet's drift motion. Over time, this motion gradually diminishes due to the damping effect exerted by viscous stress. The trajectory of the droplet, observed in both models, displays a self-similar fractal structure and eventually reaches equilibrium, where the mean squared displacement (MSD) satisfies $\langle \Delta \boldsymbol{X}^2 \rangle \sim 2D^*t$; see green lines in Figs. 5(I)(c) and 5(II)(c). Concurrently, the fourth cumulant $\langle \Delta \boldsymbol{X}^4 \rangle$ gradually increases with time t. Over a prolonged time span, it is observed that $\langle \Delta \boldsymbol{X}^4 \rangle \sim t^2$, akin to the findings reported in Ref. [49]:

$$\langle \Delta \boldsymbol{X}^4 \rangle \approx 12\,\mathrm{Var}(D^*)\,t^2,$$

where $\mathrm{Var}(D^*)$ is the variance of D^*. The displacement distribution observed in the simulations adheres to a Gaussian distribution, as depicted in Fig. 5(b). This observation suggests that the time-varying nonconstant Brownian coefficient D^* is influenced by a mechanism distinct from the diffusing-diffusivity models [50]. Further comprehension of this phenomenon unveils that the deformable droplet deviates from its originally perfect spherical shape, which introduces a nonzero variance in the Brownian coefficient. Furthermore, since each molecule within the droplet experiences random perturbations at each time step, the Brownian coefficient of the entire droplet becomes a time series that conforms to a Gaussian distribution with $\mathrm{Var}(D^*) > 0$, as per the central limit theorem. Conversely for a rigid body, every molecule experiences the same noise at each time point, resulting in a zero variance for D^*.

(III) Underdamped ballistic motion: with a further reduction in We, the composition fluctuation induced Marangoni flow dominates. Once accelerated, the droplet can be slowed down neither by the diffusion nor by the viscous stress, resulting in the ballistic motion. For both CHNS and ACNS models, we observe that the short-time MSD ($t < 0.1$) shows

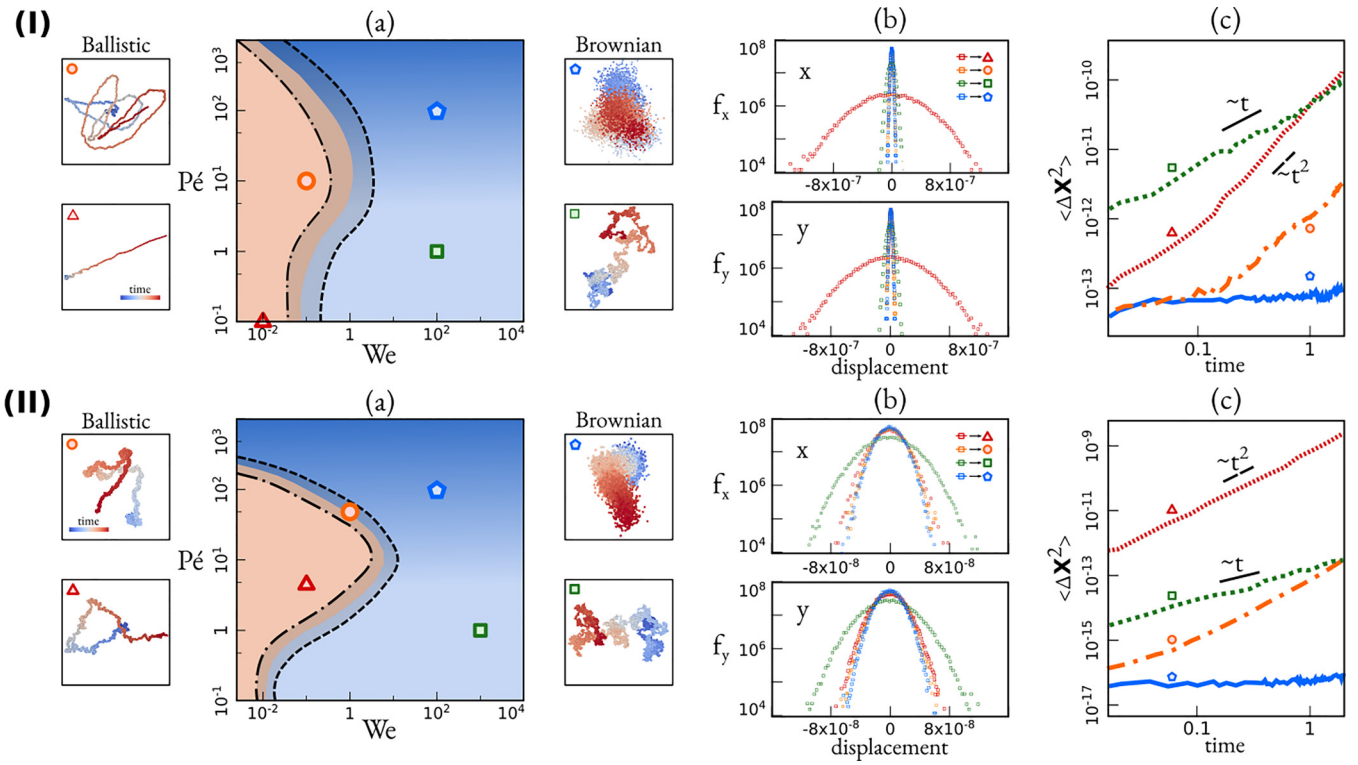

FIG. 5. The phase diagram of BM with various Weber number We and Péclet number Pe. The initial radius is $r_0 = 20$. (I) ACNS model with the noise amplitude is $\xi_\phi = 0.01$. (a) The motion phase diagram. The dot-dashed line and the dashed line separate the ballistic motion region (orange) from the no-drift Brownian region (blue) and the Brownian motion with drift region (light blue). The light gray region in between the dashed and dot-dashed lines show the transition area. Some exemplary motion trajectories are shown around pentagon-no-drift BM, square-BM with drift, triangle-ballistic motion, and circle-transition region. (b) The probability density function (PDF) of the droplet displacement. (c) MSD $\langle \Delta \boldsymbol{X}^2 \rangle$ of the example simulations with time. (II) CHNS model with the noise amplitude is $\xi_c = 0.01$.

the diffusion or subdiffusion relation with time. The droplet motion range reduces with the increase in Pe, as illustrated by the y intercept of MSD in Figs. 5(I)(c) and 5(II)(c). The later long-time behavior is vastly influenced by the composition noise induced Marangoni flow which is noticed by the steepening slope of MSD with a decrease in We.

3. *Fluctuation-induced droplet coalescence*

In this part, we report another nonequilibrium behavior stemming from the thermal composition noises which give rise to a special noise-induced droplet coalescence mechanism. Then, a multidroplet simulation proceeds and diverse morphologies are observed due to the droplet coalescence mechanism. First, we briefly introduce the droplet coalescence mechanism which has been extensively studied by Golovin and Tanaka [51,52]. Notably, Golovin [52] introduced a scenario with dual-droplets amid the surrounding matrix. An accumulation of solute material in the gap region between the droplets leads to the nonuniform solute distribution around the droplet, generating a surface tension gradient and inducing Marangoni flow, which propels the motion of the droplets [53]. Golovin's diffusion-induced motion has been further investigated by Tanaka and other researchers, employing the Cahn-Hilliard-Navier-Stokes equation [54]. In the work of Tanaka [55] and also within our CHNS model, the utilization of a double-well potential-energy function naturally results in a droplet-matrix interface with an infinitely wide interface region represented by hyperbolic tangent functions. Hence, the concentration profiles of distinct droplets consistently overlap with one another. In the case of two coalescing droplets, this overlapping leads to an asymmetric diffusion pattern around each droplet, subsequently causing a nonuniform pressure distribution in the Navier-Stokes equation, giving rise to center-to-center droplet motion, and facilitating their coalescence.

Here, we report a coalescence mechanism distinct from the Golovin-Tanaka theory by applying the ACNS model. Since the obstacle potential is adopted to the system as Eq. (4), the composition profiles are depicted by sinusoidal functions with finite interfacial width. Therefore, in contrast with the hyperbolic tangent interface profile in the CHNS model, the ACNS model enables us to eliminate the composition overlapping in the Golovin-Tanaka mechanism and deletes the nonuniform composition-induced Marangoni effect. For the simulation setup, we position two droplets of equal radius $r_0 = 20$ symmetrically within a $N_x \times N_y = 18r \times 12r$ domain. The compositional noise with an amplitude $\xi_\phi = 0.01$ is adopted. All other parameters are identical to that in Sec. II A. The initial separation between the droplets is represented by the parameter d.

As shown in the double droplet simulations of Fig. 6(I), the phase-field variable inside the gap is uniformly distributed as $\phi_M = 0$. It implies that the surface tension force $-\phi \nabla \mu$

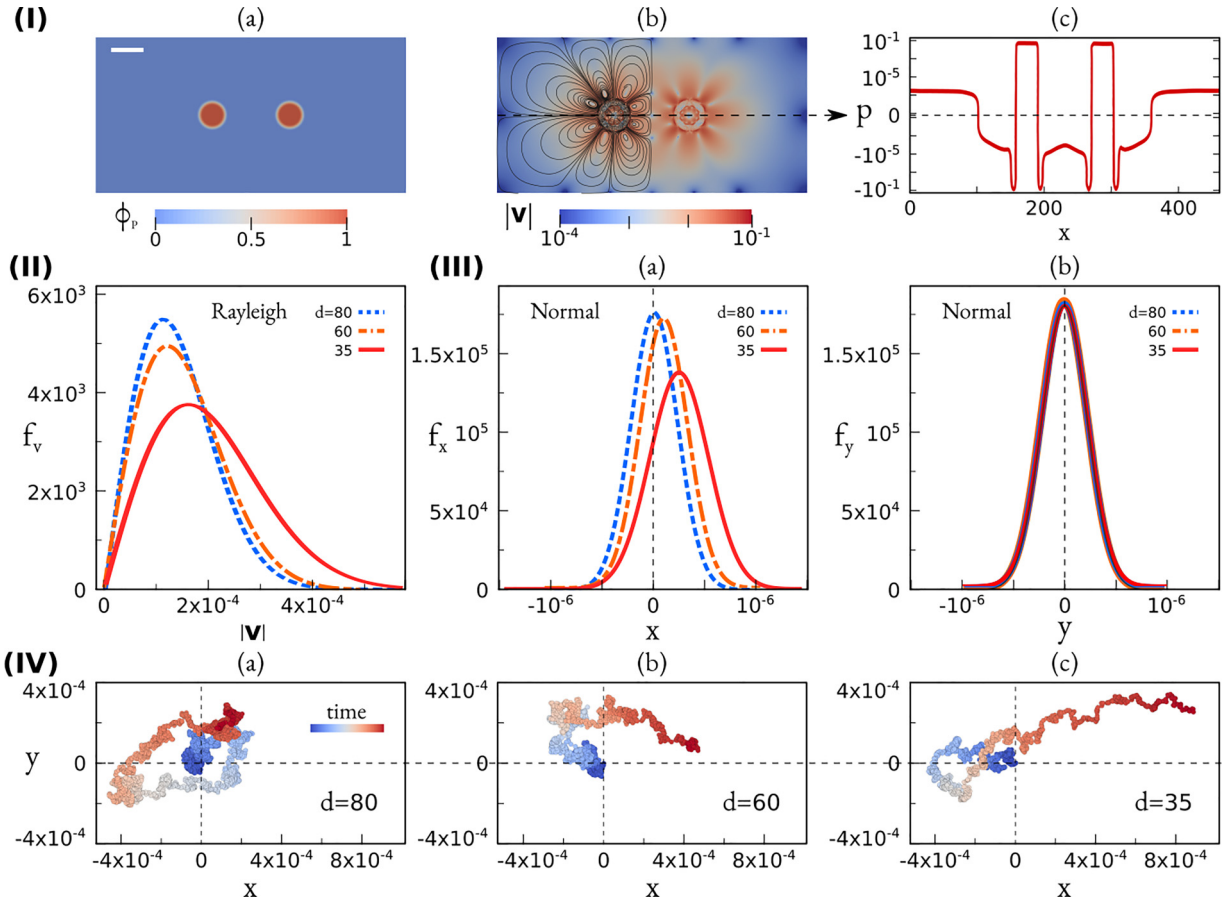

FIG. 6. 2D Brownian motion of double droplets with the same radius $r_0 = 20$ propelled by the composition noise $\xi_\phi = 0.01$. (I) The double droplet simulation with spacing at $t = 200$. (a) ϕ_P droplet order-parameter distribution. The white scale bar denotes 50. (b) The velocity field. Only the left half of the streamlines are shown and the color bar (log) scales the velocity magnitude. (c) The pressure distribution in log scale along the line of two-droplet centers. (II) The velocity and (III) displacement distributions of the left droplet changing with d. (IV) Three trajectories of the left droplet. The right shift manifests the deterministic motion. The color bar scales the time sequence.

is strictly 0 inside the gap region. In other words, the composition noise induced Marangoni effect only appears at the interface region. But the fluid flows from each interface propagate into the matrix and overlap at the droplet gap region. Clearly demonstrated in Fig. 6(II), the resulting flow velocity inside the gap region becomes larger than the outside part. Consequently, the nonuniform pressure distribution around droplets is established due to the composition noises [see Fig. 6(III)] and produces the resulting force $-\nabla p$ which propels the droplet motion.

Most importantly, the composition noise induced droplet motion in dual-droplet setup shows three significant contrasts to the single droplet simulations. (I) The droplet motion is intensified with the narrowing gap distance d. By reducing d, the probability density function (PDF) of the droplet velocity shifts towards higher velocities in Fig. 6(IV). (II) The droplet motion is anisotropic. Fitting the displacements of the left droplet in the x and y directions independently to normal distributions, the x displacement presents the apparent right shift with the reduction in d; see the middle panel of Fig. 6(IV). Contrarily, no discernible change related to droplet spacing is observed in the y direction. (III) The droplet motion is deterministic, which can be proven by two aspects. (a) The x displacement distribution shows an increase in the mean average value with reducing d in Fig. 6(IV), indicating the deterministic drift. (b) The trajectories of the left droplet in Fig. 6(V) apparently present the right-shifting motion.

Particularly, as the asymmetric velocity field results in the pressure gradient $-\nabla p$ which points inwards the gap, the deterministic droplet motions always lead to the droplet coalescence. Hence, the composition noise induced coalescence force is pure attractive and independent of the surface tension gradient. It manifests the distinction between our observation and the Golovin-Tanaka theory which indicates that the droplet coalescence always evolves to reduce the system's total surface energy. In other words, the coalescence of hydrophobic droplets cannot be explained with the Golovin-Tanaka mechanism but is indeed captured in our simulations; see the Supplemental Material, Sec. III [31] as well as the latest experiment [56]. Moreover, the coalescence force has a long-range feature, differing from the mechanism due to the short-range bridging effect at the droplet reported in Ref. [57]. An obvious proof is evident in Fig. 6(V), when the droplet spacing $d = 60$ is three times their radii, the deterministic merging can be apparently seen in the droplet trajectory.

Furthermore, we proceed with the multidroplet simulation as demonstrated in Fig. 7. The initial 50 droplets with radii $r_0 = 20$ are randomly distributed in a two-dimensional do-

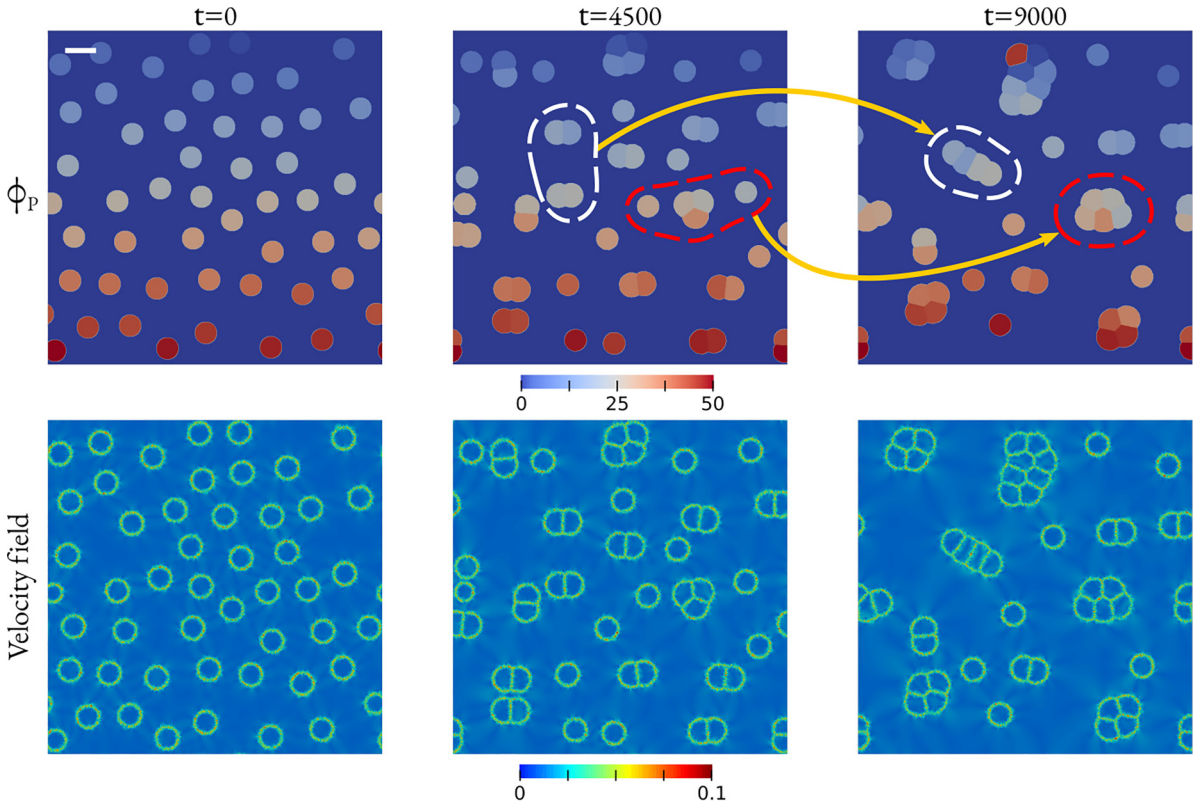

FIG. 7. The Brownian motion of multiple droplets propelled by the random composition noise fluctuation $\xi_\phi = 0.5$ for all components in the ACNS model. Upper row: 50 droplets coalescence with time. Two typical morphology transformations: (i) rod formed by Janus droplets, and (ii) big cluster via droplet collisions are highlighted with the white and red dashed curves, respectively. The underlying color bar indicates the $\boldsymbol{\phi}$ index of the system, with the first phase field variable $\phi = 0$ for the matrix and the rest numerating the 50 droplets. Lower row: velocity field around droplets scaled by the color bar beneath. The scale bar denotes the spatial length of 50.

main ($N_x = N_y = 30\, r_0$). Propelled by the composition noise with the amplitude $\xi_\phi = 0.5$ for all components, the droplet motion results in a manifest coalescence behavior, as depicted in the first row of Fig. 7. As a result of the asymmetric velocity field around the droplets, distinct multidroplet microstructures are observed, including Janus, rod, and cluster, as highlighted by the colored dashed curves in Fig. 7.

V. CONCLUSION

In conclusion, we have postulated and validated two types of stochastic phase-field models coupling with hydrodynamics to simulate the Brownian motion of droplets and droplets. Propelled by the composition fluctuations with weak Marangoni effect, the droplet-droplet proceeds the Brownian motion, depending on the amplitude of the random noise and the droplet size, and the microscopic kinetic parameter. Moreover, by altering the parameters in the Navier-Stokes equations, the stochastic phase-field models go beyond the limitation of the Langevin equation only for the rigid body and can also be utilized for soft deformable droplets. After testifying our results with the Einstein relationship within the equilibrium condition, we extend our model further into two off-equilibrium scenarios. (i) When the composition noise-induced fluid flow becomes pronounced, the transition from Brownian motion to ballistic motion is observed which indicates the noise-induced fluid flow underdamped by the viscous stress. (ii) The double droplet simulation shows a stochastic-induced deterministic droplet motion, which plays a vital role in the coalescence of the multidroplet system and is hardly considered in the Langevin dynamics. Nevertheless, in the previous Cahn-Hilliard type phase-field models [51,52], the stochastic noise terms are totally overwhelmed by the pronounced diffusion and Ostwald ripening and simply applied as a trigger for the phase separation. Here, we reevaluate the importance of the noise term and focus on the stochastic droplet motions during the coalescence process, while the subordinate Ostwald ripening effect can be neglected. Thus, the missing linkage between the coarsening droplet and the randomly drifting rigid droplet is connected. Our model is also fully implemented in three dimensions (3D). We anticipate performing large-scale three-dimensional multidroplet simulations in forthcoming research to understand the underlying mechanisms of the micro droplet motions, especially for the gelation process of soft matter materials.

ACKNOWLEDGMENTS

H.Z. thanks the Gottfried-Wilhelm Leibniz prize NE 822/31-1 of the Deutsche Forschungsgemeinschaft (DFG) for funding this research. F.W. is grateful to the VirtMat Project No. P09 of the Helmholtz Association (MSE-programme No. 43.31.01). The authors acknowledge support from the state of Baden-Wuerttemberg through bwHPC.

[1] R. Brown, A Brief Account of Microscopical Observations Made...on the Particles Contained in the Pollen of Plants, and on the General Existence of Active Molecules in Organic and Inorganic Bodies (1828).

[2] H. A. Kramers, Brownian motion in a field of force and the diffusion model of chemical reactions, Physica **7**, 284 (1940).

[3] M. C. Wang and G. E. Uhlenbeck, On the theory of the Brownian motion II, Rev. Mod. Phys. **17**, 323 (1945).

[4] P. Saffman and M. Delbrück, Brownian motion in biological membranes, Proc. Natl. Acad. Sci. USA **72**, 3111 (1975).

[5] K. N. Shukla, T. M. Koller, M. H. Rausch, and A. P. Fröba, Effective thermal conductivity of nanofluids–a new model taking into consideration Brownian motion, Int. J. Heat Mass Transfer **99**, 532 (2016).

[6] Z. Wang, J. Nie, W. Qin, Q. Hu, and B. Z. Tang, Gelation process visualized by aggregation-induced emission fluorogens, Nat. Commun. **7**, 12033 (2016).

[7] V. Baudron, P. Gurikov, and I. Smirnova, A continuous approach to the emulsion gelation method for the production of aerogel micro-particle, Colloids Surf., A **566**, 58 (2019).

[8] A. Mohraz, Interfacial routes to colloidal gelation, Curr. Opin. Colloid Interface Sci. **25**, 89 (2016).

[9] A. Zaccone, J. J. Crassous, and M. Ballauff, Colloidal gelation with variable attraction energy, J. Chem. Phys. **138**, 104908 (2013).

[10] A. Einstein, Über die von der molekularkinetischen theorie der wärme geforderte bewegung von in ruhenden flüssigkeiten suspendierten teilchen, Ann. Phys. (Berlin, Ger.) **4**, 549 (1905).

[11] J. Tóthová, G. Vasziová, L. Glod, and V. Lisỳ, Langevin theory of anomalous Brownian motion made simple, Eur. J. Phys. **32**, 645 (2011).

[12] N. Lucero-Azuara, N. Sánchez-Salas, and J. Jiménez-Aquino, Brownian motion across a magnetic field: Langevin approach revisited, Eur. J. Phys. **41**, 035807 (2020).

[13] F. Hajizadeh, L. Shao, D. Andrén, P. Johansson, H. Rubinsztein-Dunlop, and M. Käll, Brownian fluctuations of an optically rotated nanorod, Optica **4**, 746 (2017).

[14] J. Tóthová, A. Šoltỳs, and V. Lisỳ, Brownian motion in a bath responding to external electric fields, J. Mol. Liq. **317**, 113920 (2020).

[15] D. B. Mayer, E. Sarmiento-Gómez, M. A. Escobedo-Sánchez, J. P. Segovia-Gutiérrez, C. Kurzthaler, S. U. Egelhaaf, and T. Franosch, Two-dimensional Brownian motion of anisotropic dimers, Phys. Rev. E **104**, 014605 (2021).

[16] G. Lin, Z. Han, A. Shee, and C. Huepe, Noise-induced quenched disorder in dense active systems, Phys. Rev. Lett. **131**, 168301 (2023).

[17] B. Alder and T. Wainwright, Decay of the velocity autocorrelation function, Phys. Rev. A **1**, 18 (1970).

[18] S. L. Seyler and S. Pressé, Long-time persistence of hydrodynamic memory boosts microparticle transport, Phys. Rev. Res. **1**, 032003(R) (2019).

[19] G. Fier, D. Hansmann, and R. C. Buceta, Langevin equations for the run-and-tumble of swimming bacteria, Soft Matter **14**, 3945 (2018).

[20] E. W. Burkholder and J. F. Brady, Fluctuation-dissipation in active matter, J. Chem. Phys. **150**, 184901 (2019).

[21] A. Klosin, F. Oltsch, T. Harmon, A. Honigmann, F. Jülicher, A. A. Hyman, and C. Zechner, Phase separation provides a mechanism to reduce noise in cells, Science **367**, 464 (2020).

[22] Y. Shin and C. P. Brangwynne, Liquid phase condensation in cell physiology and disease, Science **357**, eaaf4382 (2017).

[23] S. Elbaum-Garfinkle, Y. Kim, K. Szczepaniak, C. C.-H. Chen, C. R. Eckmann, S. Myong, and C. P. Brangwynne, The disordered P granule protein LAF-1 drives phase separation into droplets with tunable viscosity and dynamics, Proc. Natl. Acad. Sci. USA **112**, 7189 (2015).

[24] D. S. Lee, C.-H. Choi, D. W. Sanders, L. Beckers, J. A. Riback, C. P. Brangwynne, and N. S. Wingreen, Size distributions of intracellular condensates reflect competition between coalescence and nucleation, Nat. Phys. **19**, 586 (2023).

[25] Y. Pomeau and J. Piasecki, The Langevin equation, C. R. Phys. **18**, 570 (2017).

[26] L. D. Landau and E. M. Lifshitz, *Course of Theoretical Physics* (Elsevier, Amsterdam, Netherlands, 2013).

[27] I. Steinbach, F. Pezzolla, B. Nestler, M. Seeßelberg, R. Prieler, G. J. Schmitz, and J. L. Rezende, A phase field concept for multiphase systems, Phys. D (Amsterdam, Neth.) **94**, 135 (1996).

[28] F. Wang and B. Nestler, A phase-field study on the formation of the intermetallic Al2Au phase in the Al–Au system, Acta Mater. **95**, 65 (2015).

[29] Y. Wu, F. Wang, M. Selzer, and B. Nestler, Droplets on chemically patterned surface: A local free-energy minima analysis, Phys. Rev. E **100**, 041102(R) (2019).

[30] Y. Cai, F. Wang, Z. Zhang, and B. Nestler, Phase-field investigation on the peritectic transition in Fe-C system, Acta Mater. **219**, 117223 (2021).

[31] See Supplemental Material at http://link.aps.org/supplemental/10.1103/PhysRevE.109.024208 for the non-dimensionalization process and the validation of the numerical model, which includes Refs. [58–61].

[32] P. C. Hohenberg and B. I. Halperin, Theory of dynamic critical phenomena, Rev. Mod. Phys. **49**, 435 (1977).

[33] F. Wang, A. Choudhury, C. Strassacker, and B. Nestler, Spinodal decomposition and droplets entrapment in monotectic solidification, J. Chem. Phys. **137**, 034702 (2012).

[34] H. Zhang, Y. Wu, F. Wang, F. Guo, and B. Nestler, Phase-field modeling of multiple emulsions via spinodal decomposition, Langmuir **37**, 5275 (2021).

[35] H. Zhang, F. Wang, and B. Nestler, Janus droplet formation via thermally induced phase separation: A numerical model with diffusion and convection, Langmuir **38**, 6882 (2022).

[36] M. P. A. Fisher, D. S. Fisher, and J. D. Weeks, Agreement of capillary-wave theory with exact results for the interface profile of the two-dimensional Ising model, Phys. Rev. Lett. **48**, 368 (1982).

[37] H. T. Davis, Capillary waves and the mean field theory of interfaces, J. Chem. Phys. **67**, 3636 (1977).

[38] A. Pushkarev and V. Zakharov, Turbulence of capillary waves—theory and numerical simulation, Phys. D (Amsterdam, Neth.) **135**, 98 (2000).

[39] B. Z. Shang, N. K. Voulgarakis, and J.-W. Chu, Fluctuating hydrodynamics for multiscale simulation of inhomogeneous fluids: Mapping all-atom molecular dynamics to capillary waves, J. Chem. Phys. **135**, 044111 (2011).

[40] A. Chaudhri, J. B. Bell, A. L. Garcia, and A. Donev, Modeling multiphase flow using fluctuating hydrodynamics, Phys. Rev. E **90**, 033014 (2014).

[41] F. Wang, P. Altschuh, A. M. Matz *et al.*, Phase-field study on the growth of magnesium silicide occasioned by reactive

diffusion on the surface of Si-foams, Acta Materialia **170**, 138 (2019).
[42] J. Mo and M. G. Raizen, Highly resolved Brownian motion in space and in time, Annu. Rev. Fluid Mech. **51**, 403 (2019).
[43] A. J. Ladd, Numerical simulations of particulate suspensions via a discretized Boltzmann equation. Part 2. Numerical results, J. Fluid Mech. **271**, 311 (1994).
[44] D. Nie and J. Lin, A fluctuating lattice-Boltzmann model for direct numerical simulation of particle Brownian motion, Particuology **7**, 501 (2009).
[45] M. Schmitt and H. Stark, Marangoni flow at droplet interfaces: Three-dimensional solution and applications, Phys. Fluids **28**, 012106 (2016).
[46] K. Huang and I. Szlufarska, Effect of interfaces on the nearby Brownian motion, Nat. Commun. **6**, 8558 (2015).
[47] M. Schmitt and H. Stark, Active Brownian motion of emulsion droplets: Coarsening dynamics at the interface and rotational diffusion, Eur. Phys. J. E: Soft Matter Biol. Phys. **39**, 80 (2016).
[48] Y.-J. Chen, Y. Nagamine, and K. Yoshikawa, Self-propelled motion of a droplet induced by Marangoni-driven spreading, Phys. Rev. E **80**, 016303 (2009).
[49] A. Alexandre, M. Lavaud, N. Fares, E. Millan, Y. Louyer, T. Salez, Y. Amarouchene, T. Guérin, and D. S. Dean, Non-Gaussian diffusion near surfaces, Phys. Rev. Lett. **130**, 077101 (2023).
[50] M. V. Chubynsky and G. W. Slater, Diffusing diffusivity: a model for anomalous, yet brownian, diffusion, Phys. Rev. Lett. **113**, 098302 (2014).
[51] H. Tanaka, Coarsening mechanisms of droplet spinodal decomposition in binary fluid mixtures, J. Chem. Phys. **105**, 10099 (1996).
[52] A. Golovin, A. Nir, and L. Pismen, Spontaneous motion of two droplets caused by mass transfer, Ind. Eng. Chem. Res. **34**, 3278 (1995).
[53] F. Wang, M. Selzer, and B. Nestler, On the motion of droplets driven by solutal Marangoni convection in alloy systems with a miscibility gap, Phys. D (Amsterdam, Neth.) **307**, 82 (2015).
[54] F. Wang, A. Choudhury, M. Selzer, R. Mukherjee, and B. Nestler, Effect of solutal Marangoni convection on motion, coarsening, and coalescence of droplets in a monotectic system, Phys. Rev. E **86**, 066318 (2012).
[55] R. Shimizu and H. Tanaka, A novel coarsening mechanism of droplets in immiscible fluid mixtures, Nat. Commun. **6**, 1 (2015).
[56] M. Davoodianidalik, H. Punzmann, H. Kellay, H. Xia, M. Shats, and N. Francois, Fluctuation-induced interaction in turbulent flows, Phys. Rev. Lett. **128**, 024503 (2022).
[57] S. Perumanath, M. K. Borg, M. V. Chubynsky, J. E. Sprittles, and J. M. Reese, Droplet coalescence is initiated by thermal motion, Phys. Rev. Lett. **122**, 104501 (2019).
[58] B. Nestler, H. Garcke, and B. Stinner, Multicomponent alloy solidification: Phase-field modeling and simulations, Phys. Rev. E **71**, 041609 (2005).
[59] I. Steinbach, Phase-field models in materials science, Modell. Simul. Mater. Sci. Eng. **17**, 073001 (2009).
[60] B. Uma, T. Swaminathan, R. Radhakrishnan, D. Eckmann, and P. Ayyaswamy, Nanoparticle Brownian motion and hydrodynamic interactions in the presence of flow fields, Phys. Fluids **23**, 073602 (2011).
[61] B. Nestler, F. Wendler, M. Selzer, B. Stinner, and H. Garcke, Phase-field model for multiphase systems with preserved volume fractions, Phys. Rev. E **78**, 011604 (2008).